PHYSICS OF FLUIDS **26**, 035103 (2014)

Bedload transport by a vertical jet impinging upon sediments

Bruce R. Sutherland[1,a)] and Stuart Dalziel[2]
[1]*Department of Physics, University of Alberta, Edmonton, Alberta T6G 2E1, Canada and Department of Earth and Atmospheric Sciences, University of Alberta, Edmonton, Alberta T6G 2E3, Canada*
[2]*Department of Applied Mathematics and Theoretical Physics, University of Cambridge, Cambridge CB3, United Kingdom*

(Received 23 October 2013; accepted 24 February 2014; published online 13 March 2014)

Laboratory experiments are performed to examine the formation of a crater in sediment by an impinging vertical turbulent jet. Light attenuation and a "depositometer," which records conductivity through the bed from an array of electrodes, are used to measure the crater depth as a function of space and time. The onset of crater formation and deepening is best characterized in terms of the Rouse number, Rs (proportional to the particle settling speed divided by the centerline jet speed), rather than Shields number, Sh (proportional to the stress divided by the particle weight per unit area). The critical Rouse number, Rs_c, is found to increase with the particle Reynolds number, Re_p, as a power law with exponent 0.45 ± 0.03 for Re_p ranging between 0.6 and 160. For smaller Rs, the crater is observed to deepen at a near-constant speed, while the crater radius remains constant. Bedload transport, measured in terms of the crater deepening speed, is determined to increase as Re_p times the difference between Rs_c and Rs. © *2014 AIP Publishing LLC*. [http://dx.doi.org/10.1063/1.4867707]

I. INTRODUCTION

The resuspension and transport of particles by turbulent flow has wide ranging applications in industry and the environment including the removal of micro-sized particles on surfaces by turbulent jets and channel flows,[1–7] the release of radioactive material following a nuclear accident,[8] the suspension of aerosols by wind,[9] the bedload transport of sediments by dredging or naturally by rivers and coastal currents,[10–15] and by surface and internal waves.[16–18] The diversity of phenomena and the complexities of turbulence interacting with boundaries and the motion of particles in fluid pose a continuing challenge for theorists, experimentalists, and numerical modelers.[19–23]

In environmental studies of uniform, statistically steady turbulent flow over a particle bed, the bedload transport and resuspension of particles is often characterized in terms of the Shields parameter, Sh, which represents the ratio of stress due to flow over the particle bed relative to the weight per area of the individual particles in the bed.[24] Bedload transport occurs if the Shields parameter exceeds a critical value, which depends upon particle size, shape, cohesion and buoyancy.[12,14,15] Greater particle resuspension occurs as the Shields parameter becomes larger. The critical Shields parameter itself is difficult to determine experimentally,[11,21] in part because the microscopic dynamics of particle resuspension occurs transiently due to turbulent fluctuations.

An alternate classification of sediment resuspension and settling is expressed in terms of the Rouse number, Rs, which is proportional to the ratio of the settling speed and turbulent shear velocity at the bed. Below a critical value of the Rouse number, the flow is able to maintain particles in suspension because turbulent velocity fluctuations are larger than the terminal velocity of each particle. Unlike the Shields number, the Rouse number accounts for the influence of viscosity upon

a)Email: bruce.sutherland@ualberta.ca; URL: www.ualberta.ca/~bsuther.

each particle through the value of the settling speed. Whether the Shields or Rouse number is more suitable to describe bedload transport depends upon the particle Reynolds number, Re_p, based upon the particle settling speed and diameter. It also depends upon the nature of the turbulent flow. Extensive studies have been performed to classify sediment transport by uniform, statistically steady turbulent flows in terms of the Shields and Rouse numbers. But it is not so well understood how these parameters can be used to predict resuspension onset and particle transport in transient and inhomogeneous turbulence and from coherent structures in such flows.

Several idealized experiments have been performed to examine the resuspension of particles from coherent structures in the form of vortex rings.[25–28] In the study by Eames and Dalziel,[26] a vortex ring resulted from the detachment of a wake vortex behind a sphere that impulsively stopped when impacting a surface. The vortex passed around the sphere and then along the floor lifting particles along its front. Resuspension was characterized in terms of the "particle" Shields parameter based upon the speed of the incident sphere and the reduced gravity of the particles. For small particles with $\mathrm{Re}_p \lesssim 1$, the critical Shields parameter, Sh_c, was found to be a function of particle Reynolds number with $\mathrm{Sh_c} \propto \mathrm{Re_p}^{-1/2}$. Otherwise, the critical Shields parameter was $\mathrm{Sh}_c \simeq 3.0$.

Even without the sphere, particles can be resuspended by a vortex ring impacting a sediment bed.[25] Measurements taken through light attenuation[27] and particle image velocimetry[28] showed qualitatively similar dependence of Sh_c upon Re_p, though the values of Sh_c were an order of magnitude higher than the empirical prediction for resuspension by an impacting sphere, particularly at small Re_p. The crater that formed in a bed of glass ballotini following interaction with the vortex ring was not axisymmetric, but had radially extending spokes of elevated depth resulting from azimuthal instabilities of the vortex ring upon impact. The erosion efficiency, characterized in terms of the ratio of potential energy gain of the crater to incident kinetic energy of the vortex ring, was found to have a power law dependence with an order unity exponent that varied depending upon particle size.

The focus of the present study is upon particle transport by a vertical jet impinging downward upon a sediment bed. The study differs from experimental work examining the cleaning of fine particles from a surface[1,2,6] in that the sediment bed is thick, and so the jet acts to form a crater. Thus transport is dictated by flow-particle and particle-particle interactions. Interactions between particles and the substrate are unimportant. Unlike the vortex-ring studies, here the impacting flow is fully turbulent (although inhomogeneous) and lacking in large-scale coherent structures. The intent is to examine what factors determine how a statistically steady, non-uniform turbulent flow initiates sediment transport and to measure crater formation and bedload transport as a function of the jet and particle parameters. This idealized work constitutes the first stage in a research program to understand better industrial processes such as dredging and marine biological processes such as burrowing by shellfish.

In Sec. II, we describe the experimental setup and measurement methods. Two different setups are employed. In one, crater formation onset and evolution is measured through light attenuation through the sediment bed.[29] In the other, conductivity from each electrode in a square array underlying the bed is used to measure sediment depth.[30] The analysis methods used to determine the crater deepening speed and lateral extent are described in Sec. III. Empirical predictions for crater formation onset, bedload transport and crater structure are presented in Sec. IV. Section V presents a summary of results.

II. EXPERIMENT SETUP

Here we describe the setup of the experiment along with the "depositometer" and light attenuation methods used to measure the crater depth.

A. Tank setup

The experiments were performed in two different tanks, each employing a different technique for measuring sediment depth: one uses the depositometer;[30] the other uses light attenuation.[29] A schematic of the set-up applicable for both experimental methods is shown in Figure 1.

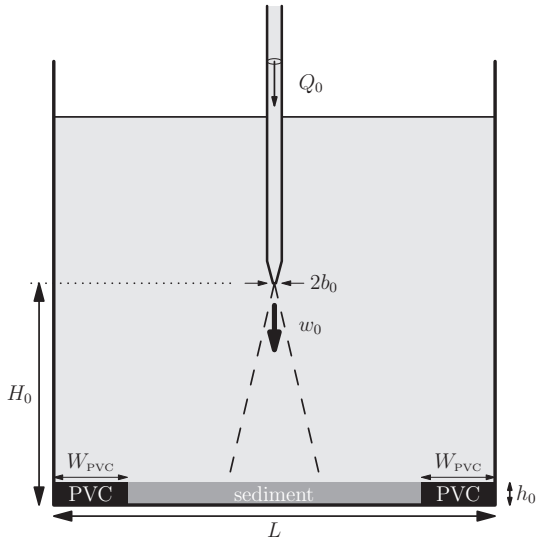

FIG. 1. Schematic of a side-view of the experiment showing a jet of fresh water injected with volume flux Q_0 through a nozzle of radius b_0 into a tank filled with fresh water. The speed of fluid exiting the nozzle is w_0. The turbulent jet widens with distance from the nozzle as indicated by the long dashed lines. The nozzle is situated a distance H_0 above the tank bottom. Two strips of PVC (black) of thickness h_0 resting on the tank bottom are situated on either side of the tank. Between these strips lies a bed of particles (dark gray) of near uniform size. Before an experiment, a scraper running along the PVC strips ensures the depth of the particle bed between the strips has depth h_0.

The depositometer experiments were performed in an acrylic tank with square horizontal cross-section, $L = 40$ cm on each side, and with height 55 cm. The bottom of the tank was fitted with an electrode array, as shown in Figure 2(a). Details of the operation of the depositometer are given in Sec. II B.

The light attenuation experiments were performed in an acrylic tank with square horizontal cross-section, $L = 30$ cm on each side, and with height 39 cm. The bottom of this tank was clear acrylic, allowing the experiment to be illuminated from underneath. Details of the light attenuation method are given in Sec. II C.

In both experiments, the tank was filled with fresh water of density $\rho_w \simeq 0.9982$ g/cm^3 to approximately 20 cm depth. Two rectangular strips of PVC that spanned the interior length of the tank were placed on the bottom of the tank against the right and left sides. The PVC strips each had width $W_{\rm PVC} = 10$ cm for the depositometer experiments and had width $W_{\rm PVC} = 5$ cm for the light attenuation experiments. The thickness of the strips was used to set the depth, h_0, of the bed of sediment either for calibration purposes or for the experiment itself. For typical experiments, $h_0 = 0.4$ cm.

A bed of approximately uniform diameter spherical particles filled the space between the PVC strips. A scraper supported by the PVC strips on either side of the particle bed was passed gently over the bed to ensure it had near uniform depth, h_0, equal to the thickness of the strips. One of four different types of particles were used in each experiment. Three of these were glass ballotini of density $\rho_p \simeq 2.5$ g/cm^3 and diameter $d_p \simeq 0.009$, 0.025, and 0.100 cm. To explore the effect of particle density upon crater formation, we also performed some experiments with white poppy seeds having mean density $\rho_p \simeq 1.39$ g/cm^3 and diameter $d_p \simeq 0.100$ cm. The properties of these particles and their relative settling speeds are given in Table I.

A jet was established by a Manostat peristaltic pump that generated flow rates between $Q_0 = 1.83$ and 7.79 cm^3/s. The flow rates were sufficiently fast that pulsations associated with the peristaltic pump action were not evident in the jet itself. The pump drew fresh water from a reservoir and injected it vertically downward into the tank after passing through a nozzle of radius $b_0 = 0.25$ cm, which was fitted with a fine mesh having openings of 0.05 cm to ensure the flow was turbulent at the source. Based on the nozzle radius and mean flow speed, the Reynolds number of

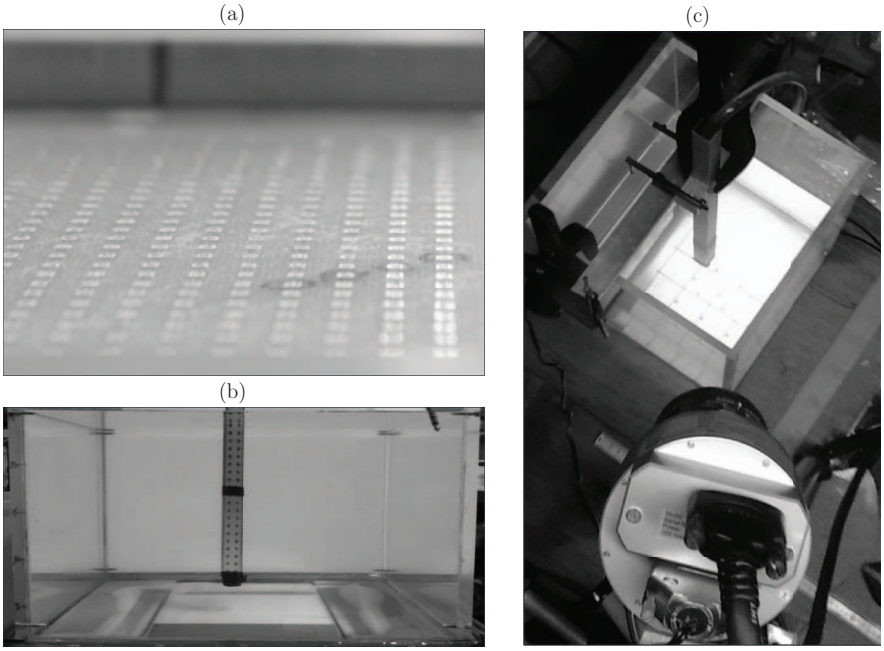

FIG. 2. Setup for experiments with sediment depth measured by depositometer and light attenuation: (a) perspective side view of depositometer electrodes at base of tank; (b) perspective side view of nozzle situated above bed of particles in depositometer experiments; (c) perspective top view of camera looking down upon nozzle situated above bed of particles in light attenuation experiments.

the flow leaving the nozzle ranged from 230 to 992. In test experiments the injected fluid was dyed, confirming the flow was indeed turbulent. The nozzle tip was situated above the bottom of the tank by a distance H_0, which varied between 4.0 and 9.0 cm from experiment to experiment.

At the start of an experiment the pump was turned on, which immediately established a volume flux Q_0 through the nozzle tip. For qualitative analysis, cameras recorded the experiment looking downward through the front side of the tank, while the back was illuminated by an electroluminescent sheet. An example of an image taken in this way at the start of an experiment is shown in Figure 2(b).

B. Depositometer measurements

The measurement of the sediment depth during a depositometer experiment did not require a camera. Instead, the depth was determined by measurements taken by an array of electrodes at the bottom of the tank, as shown in Figure 2(a). This approach employed the adaptation by Munro and Dalziel (personal communication)[37] of the method pioneered by Rooij *et al.*[30] A single square wave pulse with a ± 5 V range was sequentially passed to each electrode with a duration of 10^{-4} s. The peak-to-peak voltage between each electrode and a ground decreased when passing through water

TABLE I. Mean diameter (d_p), density (ρ_p), and measured terminal settling speed (w_p) of particles used in these experiments. Actual diameters vary about the mean by 10% and settling speeds vary about the mean by 20%. Also provided are the computed particle Reynolds number based on the measured settling speed (Re_p, defined by (15)) and the ratios of w_p to the Stokes settling speed (W_S, defined by (10)) and the characteristic inertial settling speed (W_i, defined by (13)).

Particle type	d_p (cm)	ρ_p (g/cm^3)	w_p (cm/s)	Re_p	w_p/W_S	w_p/W_i
Ballotini	0.009	2.5	0.77	0.69	1.16	0.21
Ballotini	0.025	2.5	3.74	9.35	0.73	0.62
Ballotini	0.100	2.5	15.8	158	0.19	1.30
Poppy seeds	0.100	1.39	5.0	50	0.24	0.81

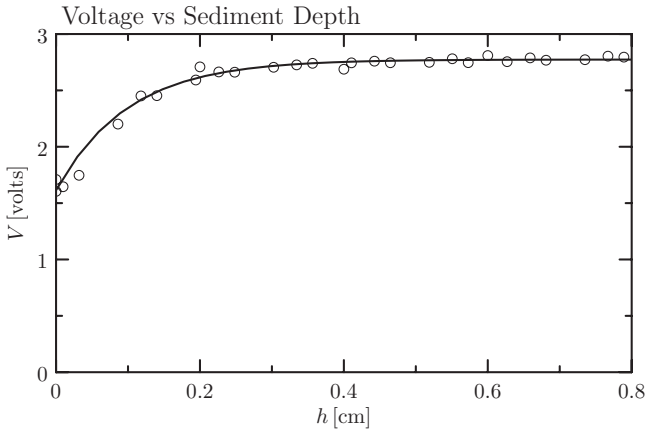

FIG. 3. Measurements of voltage, V, from probe underlying sediment of depth, h (circles) and best-fit curve of the form given by (1) with $V_0 = 1.61$ V, $V_f = 2.77$ V, $\sigma_{hv} = 0.100$ cm.

and the sediment bed. Because the voltage decrease was dominated by the sediment overlying each electrode, it was possible to calibrate the instrument to relate voltage to sediment depth, as discussed below.

The spatial resolution of measurements of sediment depth was set by the spacing between electrodes. In the experiments reported upon here, the electrodes were situated in a square array with 0.508 cm between electrode centres. In the study of crater formation, axisymmetry was assumed. Thus, if the center of the crater was not directly above any one electrode, the sediment depth was measured as function of non-uniformly spaced values of the radius, r, from the crater center to each electrode.

To calibrate the instrument, the voltage measured by each electrode was compared to a known depth of sediment above it. Measurements were taken from all electrodes with no sediment present, and with uniform-depth sediment beds with $h_0 = 0.2$, 0.4, and 0.6 cm. The sediment bed was also established with linearly decreasing depth from the front to back and from the left to right of the tank. The bedform slope was set to be approximately 0.1. The cumulation of all these measurements of voltage, V, versus depth, h, is shown in Figure 3. The measurements taken for sediment with a depth-gradient were found to be well interspersed with measurements taken for uniform-depth sediment, confirming that each electrode well measures the depth immediately above it.

The voltage was found to increase asymptotically to a saturation voltage V_f as the depth increased. Explicitly, the calibration points were found to lie along an exponential curve given by

$$V = V_f - (V_f - V_0)e^{-h/\sigma_{hv}}. \tag{1}$$

In practice, the value V_f was determined by the average of the voltages measured from electrodes underlying sediment with depth greater than 0.5 cm. The values of V_0 and σ_{hv} were then determined from the slope and intercept of the best-fit line passing through a plot of $\ln[(V - V_f)/(V_f - V_0)]$ versus h. For the calibration shown in Figure 3, the measured values were $V_0 = 1.61$ V, $V_f = 2.77$ V, and $\sigma_{hv} = 0.100$ cm.

For the four different particles used in our experiments, the saturation voltage was reached for $d \gtrsim 0.4$ cm. Thus, although the depositometer could be used to measure the deepening of a crater, it was less accurate when measuring the increase of sediment depth at the lip of the crater if the mean sediment depth was larger than a millimeter. Experiments using the light attenuation method overcame this deficiency.

C. Light attenuation measurements

Because a bed of glass ballotini is translucent, the change in light intensity passing through the bed can be related to the depth of the bed.[29] A picture of the experimental setup is shown in

Figure 2(c). A digital camera (Vosskuhle, CCD-1300QFR, 1024x1024 pixel, 8 bit grayscale) was situated above the top corner of the tank looking through the tank surface to the bottom. A perspective view was necessary to view the tank bottom directly beneath the jet nozzle situated a distance H_0 above. The tank itself was illuminated from underneath by an array of fluorescent lamps shining upon an angled mirror.

The image in Figure 2(c) shows the camera recording a grid of lines spaced by 5 cm drawn on a transparent sheet lying on the tank bottom. This was used to establish a world co-ordinate mapping. With the camera held in place, the transparent sheet was removed and a bed of ballotini particles was added. As for the calibration of the depositometer, the light intensity was recorded with no particles, with the particle bed having uniform depth of 0.2 and 0.4 cm, and with the depth of the particle bed decreasing linearly from left to right and from the front to back of the tank.

For the $d_p = 0.009$ cm and 0.025 cm diameter ballotini and with a slightly blurred image, there were a sufficient number of particles in an image pixel (with dimensions on the order 0.03 cm $\times$ 0.03 cm) that there was little noise in the light signal due to internal reflections within the medium.[31] As expected for these particles, the intensity was found to decrease exponentially with increasing depth, asymptotically approaching the "black" intensity $I_b = 40$, with white being 255. (The true black intensity for the camera was 8, but I_b was larger due to ambient light.) In particular, for a bed of 0.009 cm diameter ballotini, the relationship between intensity, I, and depth, h, was found to be

$$I = I_b + (I_0 - I_b)e^{-h/\sigma_{hI}} \tag{2}$$

with $I_b = 40$, $I_0 = 249$, and $\sigma_{hI} = 0.351$ cm.

III. ANALYSIS METHODS

Here we present the qualitative results of depositometer and light attenuation experiments and we explain how measurements of sediment depth as a function of radius and time are analyzed to characterize the crater extent, the deepening rate of the centre and the growth rate and extent of the crater lip.

Figure 4 shows the evolution of a crater recorded in a light attenuation experiment. Here the $h_0 = 0.40$ cm deep bed is composed of ballotini with diameter $d_p = 0.009$ cm. The nozzle is situated $H_0 = 5.0$ cm above the tank bottom and the volume flux at the source is $Q_0 = 6.03$ cm^3/s.

At the start of the experiment, the top camera recorded near-uniform intensity of light from the uniform-depth of particles below the nozzle (Figure 4(a), left). As the jet continually impacted the sediment bed, particles were transiently swept away from the centre. At time $t = 50$ s (Figure 4(b)) the beginning of the formation of a crater became evident. The image appears brighter directly underneath the nozzle and a darker halo is visible around the centre. In these images and in images at a later time, a black cross is evident. This was drawn at the centre of the bottom of the tank to indicate the approximate location of the center of the impacting jet.

At successive times the crater continued to deepen and the crater lip grew as evident, respectively, by brighter and darker regions in the image. In this experiment, the crater exposed the bottom of the tank at time $t \simeq 180$ s. Thereafter, the crater lip continued to grow, while the area of the exposed region widened (Figure 4(e)). The crater remained essentially axisymmetric in all our experiments, showing no evidence of radially extending regions of scouring and enhanced depth that were observed in experiments of crater formation by an impacting vortex ring.[27,28]

Radial time series of the sediment depth were measured from both depositometer data and from light attenuation experiments. The results of a typical depositometer experiment are shown in Figure 5(a). In this experiment, a $h_0 = 0.4$ cm deep bed of 0.009 cm diameter ballotini lay below under a jet with volume flux $Q_0 = 6.68$ cm^3/s and nozzle situated $H_0 = 5.0$ cm above the tank bottom.

The time series shows how the depth, h, of sediment above probes at different radii from the crater center decreased in time. As evident in Figure 5(a), data exist at irregularly spaced values of $r = r_{e1}, r_{e2}, r_{e3}, \ldots$, with the electrode closest to the crater center being situated at r_{e1} and with $r_{e1} < r_{e2} < r_{e3} < \ldots$ denoting the successive radii of electrodes from the crater center. For the experiment

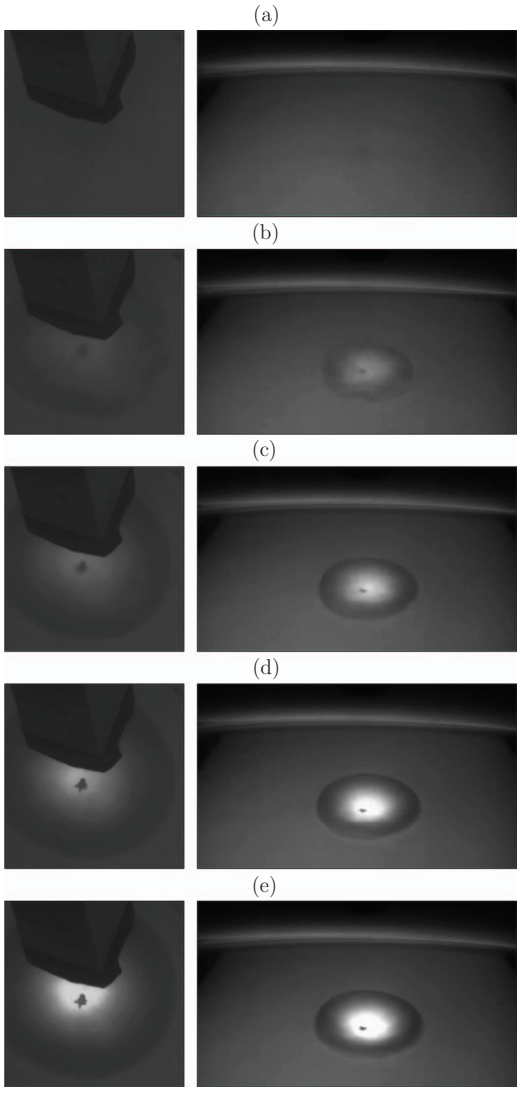

FIG. 4. Snapshots taken every 50 s from the start of a light-attenuation experiment. The left images are close-up of snapshots taken by the top perspective camera, which is later used to measure sediment depth by light attenuation. The right images are extracted from a movie taken by a side perspective camera. Experiment parameters are $H_0 = 5.0$ cm, $Q_0 = 6.03$ cm^3/s, $h_0 = 0.40$ cm, $d_p = 0.0090$ cm, and $\rho_p = 2.5$ g/cm^3. (a) t = 0 s; (b) t = 50 s; (c) t = 100 s; (d) t = 150 s; and (e) t = 200 s.

shown in Figure 5, $r_{e1} = 0.21$ cm. To fill out the radial time series plot, at a fixed time t and at some radius r such that $r_{en} < r < r_{e(n+1)}$, $h(r, t)$ is taken to equal $h(r_{e(n+1)})$. For $r < r_{e1}$, $h(r, t)$ is taken to equal $h(r_{e1})$.

From these results we determined the radial extent of the crater, $r_0(t)$, and the depth of the crater at its center, $d_c(t) = h_0 - h(r = 0, t)$. Both quantities were measured by finding at each time the best-fit parabola of the form

$$\mathcal{A}r^2 + \mathcal{C} \tag{3}$$

to $h(r, t)$ data, with the fit being applied only at times for which the crater had deepened sufficiently. Explicitly, for each time we defined $h_{1/2} = [h_0 + h(r_{e1}; t)]/2$ and we determined the number of electrodes, n, for which $h(r_{en}; t) < h_{1/2}$. The parabolic fit was determined only if $h(r_{e1}) < 0.95h_0$ and $n > 2$. For example, the best-fit parabola through $h(r, t)$ data at time $t = 100$ s is shown as the dashed line in Figure 5(b).

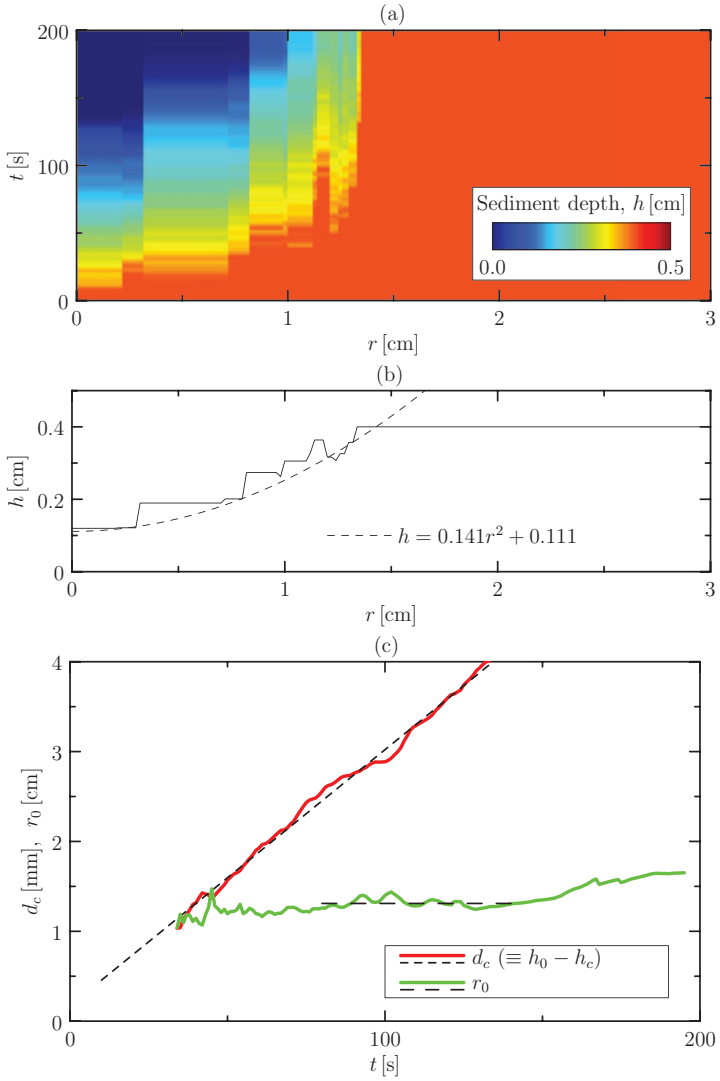

FIG. 5. Depositometer measurements used to produce (a) radial time series of sediment depth, h, (b) sediment depth versus radius at time $t = 100$ s (solid) with best-fit parabola (dashed), and (c) the crater depth at its center, $d_c \equiv h_0 - h_c$, (red) and its radius, r_0, (green) versus time. Here $h_c \equiv h(r = 0, t)$ is the depth of sediment at the crater center. Note that d_c is given in units of mm, whereas r_0 is given in cm. The best-fit line through $d(t)$ for $40 \le t \le 140$ s is shown by the short-dashed line. The mean radius for $80 \le t \le 140$ s is shown by the long-dashed line. Experiment parameters are $H_0 = 5.0$ cm, $Q_0 = 6.68$ cm^3/s, $h_0 = 0.40$ cm, $d_p = 0.0090$ cm, and $\rho_p = 2.5$ g/cm^3.

The best-fit at each time gave values for the coefficients $\mathcal{A}$ and $\mathcal{C}$. The depth of the crater at its center was thus estimated to be

$$d_c(t) = h_0 - \mathcal{C}. \tag{4}$$

The radius of curvature at the center of the crater was estimated to be $r_c = 1/(2\mathcal{A})$. As a more intuitive measure of the crater's radial extent we define

$$r_0(t) = \left[r_c{}^2 - (r_c - d_c)^2\right]^{1/2} = \left[2r_c d_c - d_c{}^2\right]^{1/2}, \tag{5}$$

which is the half-length of a chord of a circle of radius r_c whose closest distance to the circle's center is $r_c - d_c$. That is, if the crater was a hemispherical cap penetrating into the sediment layer, then r_0 would be the horizontal radius of the cap. If $r_c \gg d_c$, which is generally the case, this is approximately equal to the radius, $(2r_c d_c)^{1/2}$, of a paraboloid penetrating into the sediment layer.

The crater radius and center-depth computed in this way from the radial time series in Figure 5(a) are plotted as a function of time in Figure 5(c).

The thick red line shows that the crater depth increased almost linearly in time after it had deepened sufficiently (after time $t = 34$ s for which $d_c = 0.10$ cm). The short-dashed line represents the best-fit line through $d_c(t)$. Its slope gives the crater deepening rate $w_c = d\,d_c/dt \simeq 0.0029$ cm/s.

The thick green line shows that the crater radius was almost constant in time after it had deepened sufficiently but before the bottom had become exposed. The long-dashed line represents the mean radius over times between $t = 80$ and 140 s. Its value is $\overline{r_0} = 1.31$ (± 0.05) cm. For $t > 140$ s, the tank bottom became exposed ($d_c(t) = h_0$) in this experiment. The plot of $r_0(t)$ in Figure 5(c) shows that the crater radius continued to increase in time after bottoming out. Our focus here, however, is upon processes taking place up to the time that the crater deepened to the full sediment layer depth.

The analysis methods were similar when applied to light attenuation data, as shown in Figure 6. These results are extracted from the experiment for which snapshots are shown in Figure 4. The experimental parameters are identical to those of the depositometer experiment analyzed in Figure 5, except that here the source volume flux is $Q_0 = 6.03$ cm^3/s. In Figure 6(a), the radial resolution of $h(r, t)$ is significantly higher than the depositometer data, though the temporal resolution (corresponding to the analysis of snapshots taken every 10 s) is lower. Because of the cross drawn on the tank bottom near the crater center, the determination of the crater depth near $r = 0$ was inaccurate. Such anomalous points were filtered before finding the best-fit parabola of the form (3) to values of $d(r, t)$ at fixed times. Otherwise, the procedure was the same.

As with the depositometer measurements, the crater depth was found to increase linearly and the radius was found to be approximately constant in time after the crater developed significantly and before the bottom of the tank became exposed. For the experiment analyzed in Figure 6, the crater depth increased at a rate $w_c = 0.0017$ cm/s and the mean radius was $\overline{r_0} = 1.21$ (± 0.04) cm.

The light attenuation method was also capable of measuring the development of the lip surrounding the crater. To measure its radius from the centre, r_ℓ and its speed of growth w_ℓ, we proceeded similar to the approach used to analyze the crater. At each time, we determined the radial position of the maximum value, $h_{\max}$, of $h(r, t)$ and we fit a parabola of the form

$$\mathcal{A}r^2 + \mathcal{B}r + \mathcal{C} \tag{6}$$

to points surrounding this location where $h > (h_0 + h_{\max})/2$, provided there were at least three such points and provided $h_{\max} > 1.02\,h_0$. The radius of the lip was estimated by the location of the maximum of the parabola

$$r_\ell(t) = -\mathcal{B}/(2\mathcal{A}). \tag{7}$$

The height of the lip above the mean depth of the sediment bed was estimated by

$$d_\ell(t) = \mathcal{C} - \mathcal{B}^2/(4\mathcal{A}) - h_0. \tag{8}$$

Finally, the width of the lip was estimated by the extent of the fit-parabola with values larger than h_0,

$$\delta_\ell(t) = 2\,(-d_\ell/\mathcal{A})^{1/2}\,. \tag{9}$$

These values are plotted as a function of time in Figure 6(c).

As with the crater's center, we found that the height of the lip increased approximately linearly in time. The best-fit line to values of $d_\ell(t)$ gave the speed of growth to be $w_\ell = 0.00027$ cm/s. Meanwhile the radius and width of the lip were approximately constant such that $r_\ell = 1.97$ (± 0.02) cm and $\delta_\ell = 0.68$ (± 0.11) cm.

From the analysis of numerous depositometer and light attenuation experiments, we characterized the properties of the crater formation through measurements of $\overline{r_0}$, w_c, $\overline{r_\ell}$, w_ℓ, and $\overline{\delta_\ell}$. In what follows we attempt to determine how these properties depend upon the experimental parameters, namely, the jet source height and flow rate (H_0 and Q_0, respectively), the initial sediment depth, h_0, and the particle diameter and density (d_p and ρ_p, respectively).

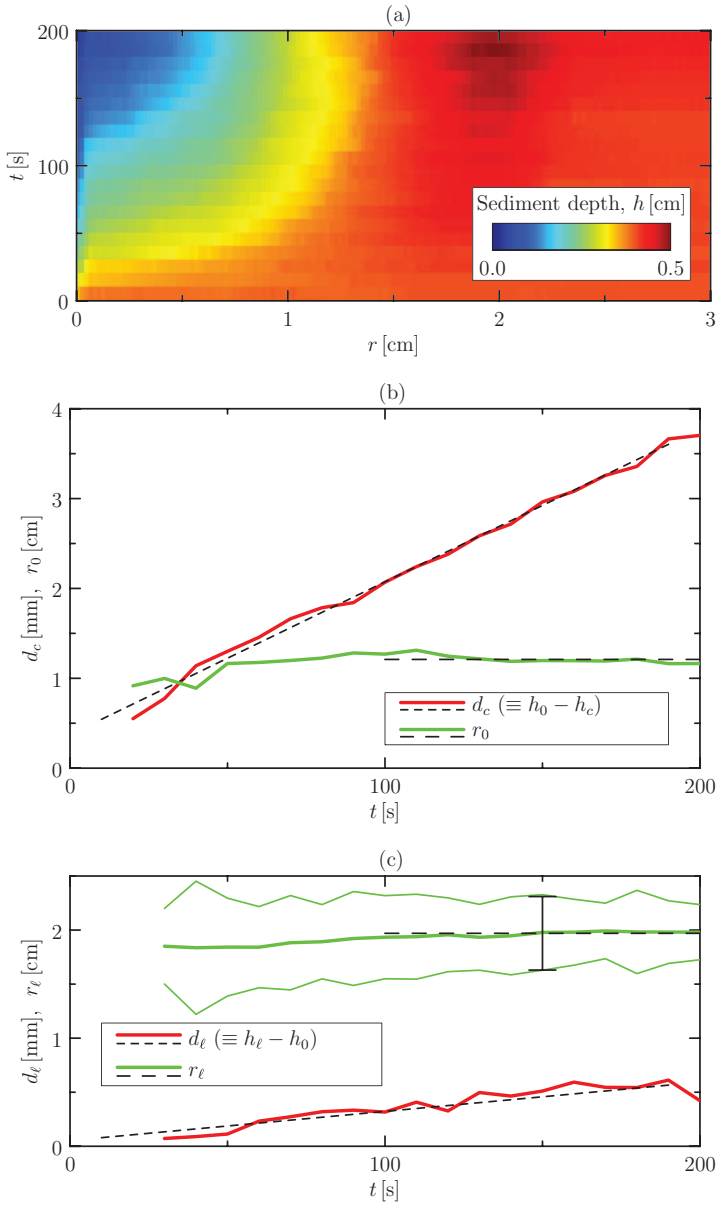

FIG. 6. Light attenuation experiments used to measure (a) radial time series of sediment depth, $h(r, t)$, (b) center depth of crater, d_c, (red) and crater radius, r_0, (green) versus time, and (c) crater lip height, $d_\ell = h_\ell - h_0$, (red) and radius, r_ℓ, from the crater center (thick green) with the radial extent of the lip, δ_ℓ indicated by thin green lines. Here, $h_\ell = h(r_\ell, t)$ is the depth of sediment at the crater lip. Note that d_c and d_ℓ are given in units of mm, whereas r_0 and r_ℓ are given in cm. In (b) the best-fit line through $d_c(t)$ for $20 \le t \le 190$ s is shown by the short-dashed line and the mean radius for $100 \le t \le 200$ s is shown by the long-dashed line. In (c) the best-fit line through $d_\ell(t)$ for $30 \le t \le 200$ s is shown by the short-dashed line, the mean radius, $\bar{r_\ell}$, for $100 \le t \le 200$ s is shown by the long-dashed line, and the error bars indicated the mean radial extent of the lip, $\bar{\delta_\ell}$ for $100 \le t \le 200$ s. Experiment parameters are the same as those in Figure 4.

IV. RESULTS

In all our experiments, whether with the depositometer or through the use of light attenuation, we found that the center of the crater, if it formed at all, deepened at an approximately constant speed, w_c. Figure 7(a) plots the normalized deepening speed, versus the Shields parameter. The deepening speed is normalized by the measured settling speed of the respective particles, w_p. This

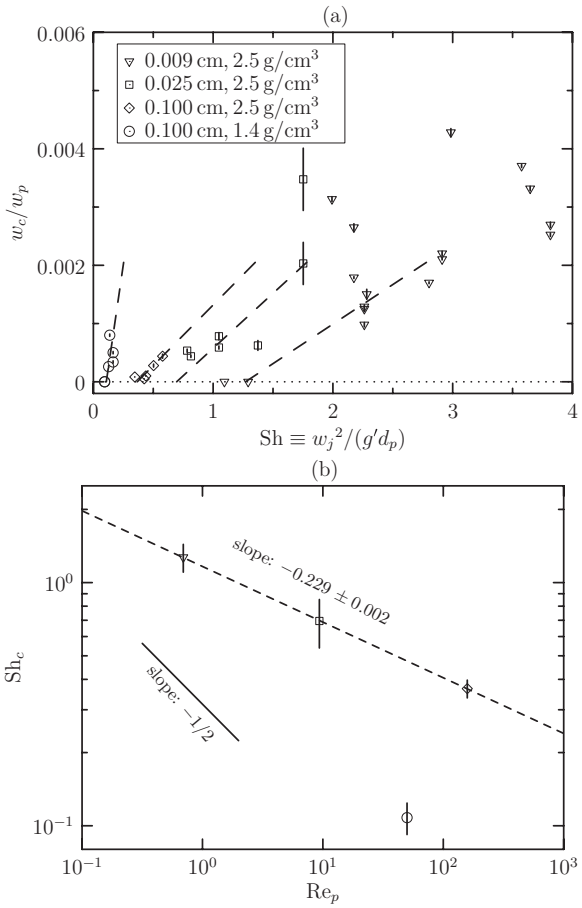

FIG. 7. (a) Normalized crater deepening speed versus the Shields parameter. Different symbols correspond to different types of particles composing the sediment, as indicated in the legend: for glass ballotini with $\rho_p = 2.5$ g/cm^3, $d_p = 0.009$ cm (down-pointing triangles), $d_p = 0.025$ cm (squares), $d_p = 0.100$ cm (diamonds); for white poppy seeds with $\rho_p = 1.4$ g/cm^3 and $d_p = 0.100$ cm (circles); the horizontal dotted line indicates where $w_c = 0$. The dashed lines show the best-fit line through data for each type of particle. The best-fit is determined only for relatively slowly deepening craters with $w_c \leq 0.002 w_p$. (b) Log-log plot of the critical Shields parameter versus particle Reynolds number. Symbols are the same as those in (a) with the vertical lines on each symbol representing the associated error. The dashed line is the best-fit line through data associated with the ballotini. The line of slope $-1/2$ is also shown.

differs from the Stokes settling speed, given by

$$W_S = \frac{g' {d_p}^2}{18\nu}, \tag{10}$$

in which d_p is the particle diameter, ν is the kinematic viscosity of water, and $g' = g(\rho_p - \rho_0)/\rho_0$ is the reduced gravity computed from the densities of the particle and water, ρ_p and ρ_0, respectively. As shown in Table I, the measured settling speed differs from W_S by 15% for the 0.009 cm diameter ballotini and is up to 5 times smaller for the largest particles due to inertial effects.

In the study of steady horizontal flow over a uniform bed of particles, the transport and suspension of particles is characterized in terms of the force per particle area induced through stress by a flow $\mathcal{U}$, divided by the weight of each particle. The stress is on the order $\rho_0 \mathcal{U}^2$. The weight per area of particle is on the order $g(\rho_p - \rho_0)d_p$. Combining these relations gives the Shields parameter,

$$\mathrm{Sh} = \mathcal{U}^2/(\mathrm{g'd_p}). \tag{11}$$

For statistically steady, turbulent but otherwise uniform flow, bedload transport is anticipated if Sh is sufficiently large.[24,28]

In our study the flow is neither steady nor uniform. Nonetheless, we may define the counterpart of the Shields parameter appropriate for flow resulting from an impinging jet,

$$\mathrm{Sh} \equiv \frac{\mathrm{w_j}^2}{\mathrm{g'd_p}}. \tag{12}$$

This can be regarded as the square of the ratio of the jet speed to the characteristic inertial settling speed,

$$W_i \equiv \sqrt{g' d_p}, \tag{13}$$

descriptive for sufficiently large particles. The value of w_j is determined from the theory for turbulent jets, reviewed in the Appendix. Explicitly, from (A5), the mean speed of the jet at the particle bed is taken to be

$$w_j = w_0 \frac{b_0}{\alpha}\left(H_0 - h_0 + \frac{b_0}{\alpha}\right)^{-1}, \tag{14}$$

in which b_0 is the nozzle radius and $w_0 = Q_0/(\pi {b_0}^2)$ is the mean speed of fluid at the nozzle expressed in terms of the source volume flux. For a jet, the entrainment constant is taken to be[32,33] $\alpha = 0.08$.

For sufficiently large Sh, the crater deepens and generally does so at a greater speed for larger Sh, although there is no obvious relationship between w_c and Sh for $w_c \gtrsim 0.002 w_p$. The dotted lines in Figure 7(a) represent the best-fit lines through data for each type of particle. The fits are constructed only for data with deepening velocities, w_c, less than $0.002 w_p$. The intercept of these lines with the axis where $w_c = 0$ are used to estimate the critical value of the Shields parameter, $\mathrm{Sh_c}$, below which no significant crater formation occurs.

In terms of the critical jet speed at the particle bed for bedload transport, w_{jc}, the critical Shields parameter is $\mathrm{Sh_c} \equiv \mathrm{w_{jc}}^2/(\mathrm{g'd_p})$. This is plotted in Figure 7(b) against the particle Reynolds number based upon the observed settling speed and the particle diameter:

$$\mathrm{Re_p} \equiv \frac{\mathrm{w_p d_p}}{\nu}. \tag{15}$$

In experiments of uniform flow over sufficiently large particles, the critical Shields parameter is found to be an approximately order-unity constant. However, viscosity plays a role when the particle size is comparable to the extent of the viscous sublayer underlying the turbulent flow.[26–28] In this case, the characteristic flow speed passing over the particles is $\mathcal{U}\mathrm{Re}$, in which $\mathrm{Re} = \mathcal{U}\mathrm{d_p}/\nu$ is the Reynolds number based upon the characteristic flow speed and particle diameter. Thus, for sufficiently small particles, the critical Shields parameter is expected to vary with the particle Reynolds number according to[27,28]

$$\mathrm{Sh_c} \sim \mathrm{Re_p}^{-1/2}. \tag{16}$$

The plot in Figure 7(b) shows that the critical Shields parameter measured for three sizes of glass ballotini decreases with increasing particle Reynolds number, but as

$$\mathrm{Sh_c} = (1.165 \pm 0.005)\mathrm{Re_p}^{-0.229\pm0.002} \tag{17}$$

instead of the predicted $-1/2$ power law. The discrepancy reflects the wide range of particle Reynolds numbers in our experiments between $\mathrm{Re}_p = 0.7$ and 160. From the experiments with white poppy seeds, the critical Shields parameter lies an order of magnitude below this curve, meaning that significantly less flow from the jet is required to initiate transport of these particles and form a crater. Indeed, observing the poppy seed experiments in progress, it is obvious that the particles are more easily resuspended into the fluid column and they remain in suspension much longer than ballotini near the critical Shields parameter. This suggests that the particle settling speed relative to the background flow speed plays an important role in setting the critical Shields parameter and in determining crater formation at supercritical Shields parameters.

Not having performed experiments with wider ranging particle sizes and densities, we are unable to make an empirical prediction for the critical Shields parameter as it depends upon ρ_p and

d_p. Instead, we reanalyze the data explicitly considering the settling speed of the particles through the Rouse number $\mathrm{Rs} = \mathrm{w_p}/(\kappa \mathrm{u}_\star)$, in which $u_\star$ is the shear (friction) velocity and $\kappa = 0.41$ is the von Kármán constant. Bedload transport in a unidirectional, statistically steady turbulent flow is anticipated[34] if $\mathrm{Rs} \lesssim 2.5$ with substantial resuspension occurring if $\mathrm{Rs} \lesssim 1$.

By analogy, we define the Rouse number for a turbulent jet impinging vertically upon a bed of particles to be

$$\mathrm{Rs} = \frac{\mathrm{w_p}}{\kappa \mathrm{w_j}}. \tag{18}$$

For very small particles, for which particles are expected to fall at the Stokes settling speed given by (10), Rs is related to Sh and Re_p by

$$\mathrm{Rs} = \frac{1}{3\sqrt{2\kappa}} \left(\frac{\mathrm{Re_p}}{\mathrm{Sh}} \right)^{1/2} \simeq 0.58 \mathrm{Re_p^{1/2} Sh^{-1/2}}. \tag{19}$$

Hence, using (16), the critical Rouse number is expected to vary with particle Reynolds number as

$$\mathrm{Rs_c} \sim \mathrm{Re_p^{3/4}}, \tag{20}$$

if $\mathrm{Re}_p \ll 1$. For large particles that fall at a speed proportional to W_i given by (13), the critical Rouse number should be independent of the particle Reynolds number and vary as the inverse square root of the critical Shields number,

$$\mathrm{Rs_c} \sim \mathrm{Sh_c^{-1/2}}. \tag{21}$$

Similar to Figure 7, Figure 8 plots the relative crater deepening speed versus the Rouse number given by (18). By comparison with Figure 7, we find a better collapse of data for each particle type, suggesting that the Rouse number, rather than Shields parameter, better determines the onset and degree of bedload transport. This is expected because the definition of the Shields parameter does not depend upon viscosity, whereas the effects of viscosity, whether significant or not, are implicitly captured by the measured settling velocity w_p and hence by the Rouse number. The intercept of the best-fit lines with the $w_c = 0$ axis, shown in Figure 8(a), gives the critical Rouse number, Rs_c. These values are plotted versus the particle Reynolds number in Figure 8(b). We find that Rs_c generally increases with increasing Re_p, with values between 0.4 and 5 from the smallest to largest ballotini. For ballotini data, the best-fit line through $\log(\mathrm{Rs}_c)$ versus $\log(\mathrm{Re}_p)$ has slope 0.45 ± 0.03, smaller than the 3/4 power law predicted by (20) for very small particles. The critical Rouse number computed for the white poppy seeds is moderately above this line, though this could be attributed to the wider spread of this data (open circles in Figure 8(a)).

Including the computed intercept of the best-fit line in Figure 8, the empirical formula for the critical Rouse number is

$$\mathrm{Rs_c} \simeq (0.58 \pm 0.05) \mathrm{Re_p^{(0.45 \pm 0.03)}}. \tag{22}$$

Putting the empirical result for the measured critical Shields parameter (17) in (19), a smaller exponent of 0.39 might be expected. The discrepancy in the exponent can be attributed to the errors in determining Sh_c.

Particularly in experiments with larger particles, there was significant error associated with the measurement of the crater radius, r_0. We analyzed the crater radius only for experiments with the 0.009 cm and 0.025 cm ballotini, for which the crater descent rate was relatively small and the radius was well-defined for long times during the crater formation. We found that the radius was reasonably represented by the radial extent of the jet at the particle bed when the flow rate exceeded the critical flow rate determined by the value of the critical Rouse number, Rs_c. From the empirical fit, given by (22), using the upper bound on the errors, we defined the critical jet speed by $w_{j\star} \simeq 0.63 \mathrm{Re_p^{0.48}}$. We suppose the time-averaged vertical flow within the jet at a distance z from the nozzle has a Gaussian structure in r with standard deviation increasing as[35] $\sigma(z) = b_0 + \alpha z$ (see the Appendix). At the surface of the sediment bed, the vertical flow exceeds the critical speed for radii less than a threshold

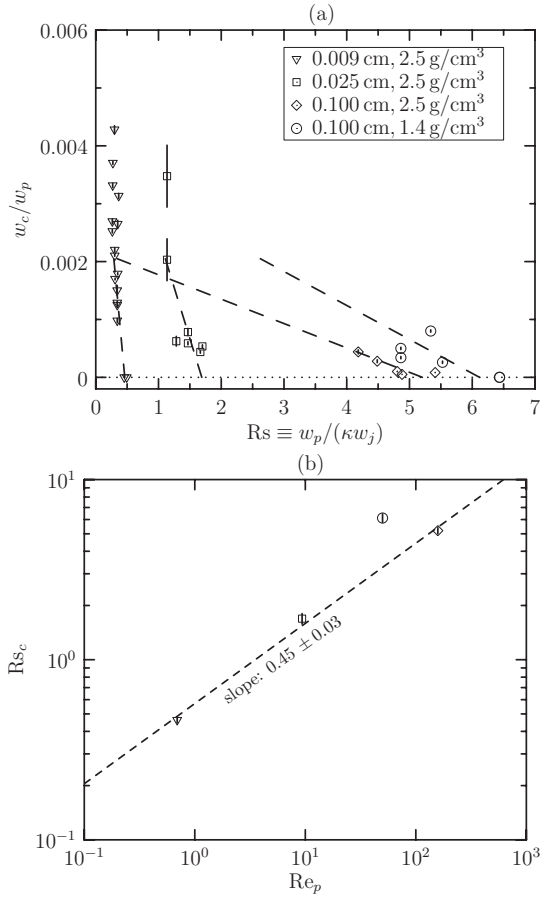

FIG. 8. (a) Relative crater deepening speed versus the Rouse number and (b) critical Rouse number versus particle Reynolds number. Symbols are the same as those shown in Figure 7(a). Error bars are indicated by vertical lines in both plots.

radius

$$r_{j\star} = \sigma(H_0 - h_0)\sqrt{2\ln(w_j/w_{j\star})}, \tag{23}$$

in which w_j is the predicted vertical speed of the jet at the centerline.

The measured crater radius, r_0, versus $r_{j\star}$, given by (23), is plotted in Figure 9. Although there is scatter in the data, the measured crater radius is consistent with the predicted critical radius within errors.

In experiments using light attenuation we measured the radius, r_ℓ, where the crater lip had maximum height, and we measured the mean radial extent δ_ℓ of the lip above the mean sediment depth. As shown in Figure 6(c), once it began to form, the crater lip had nearly constant radial extent from the center of the crater and the width of the lip was approximately constant. The number of experiments in which the lip-radius and extent could be measured above noise was limited. For these experiments, as expected, we found that r_ℓ was generally larger if the crater radius, r_0, was larger. Values of r_ℓ are plotted against the corresponding values of r_0 in Figure 10. A best-fit line through the data predicts

$$r_\ell/r_0 \simeq 1.8 \pm 0.1. \tag{24}$$

If the critical Shields parameter is exceeded or if the Rouse number is below Rs$_c$, the jet is capable of displacing particles in the sediment bed. For uniform, statistically steady turbulent flow over a sediment bed, bedload transport is characterized by the volume flux of particles per unit width of flow, Q. Typically, this is normalized by the particle size and inertial settling speed, W_i, to give

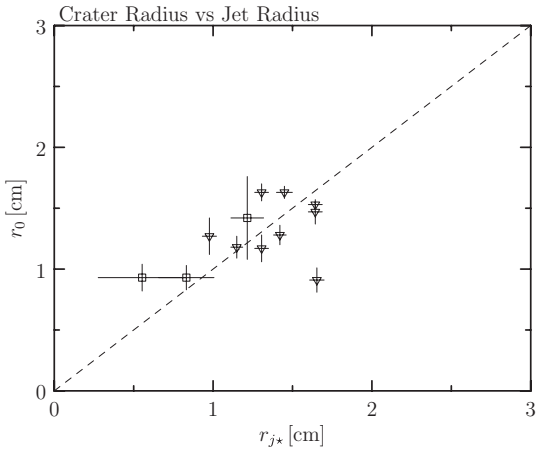

FIG. 9. Measured crater radius, r_0, versus the critical jet radius, $r_{j\star}$, below which the predicted mean vertical speed of the jet at the bed exceeds the critical speed for bedload transport, $w_{j\star}$. Data are plotted only for $d_p = 0.0090$ cm (downward triangles) and 0.025 cm (squares) ballotini. The one-to-one line is represented by the dashed line.

the nondimensional volume flux per width,[36] $\tilde{Q} = Q/(d_p W_i)$. Multiplying top and bottom by the width of the flow, L, the normalizing factor in the denominator is seen to be the particle settling flux, ${d_p}^2 W_i$, divided by the across-flow particle density, d_p/L.

Through analyses of experiments examining bedload transport by uniform flow over sediment beds, empirical formulas have been developed to relate $\tilde{Q}$ to the difference, $\mathrm{Sh} - \mathrm{Sh}_c$, with proposed formulas typically of the form

$$\tilde{Q} = \mathcal{C}_s(\mathrm{Sh} - \mathrm{Sh_c})^{\mathrm{p}}, \tag{25}$$

for constant coefficient $\mathcal{C}_s$ and exponent p. The values of $\mathcal{C}_s$ and p depend upon the particle size, density and the relative stress imposed by the flow over the particle bed.

In our experiments, the vertical descent rate of the center of the crater, w_c, is used to measure of the volume transport of sediment by the impinging jet. Explicitly, because we found that the crater radius, r_0, changed little as the crater deepened (e.g., see Figures 5(b) and 6(b)), the volume flux is

$$Q \propto {r_0}^2 w_c. \tag{26}$$

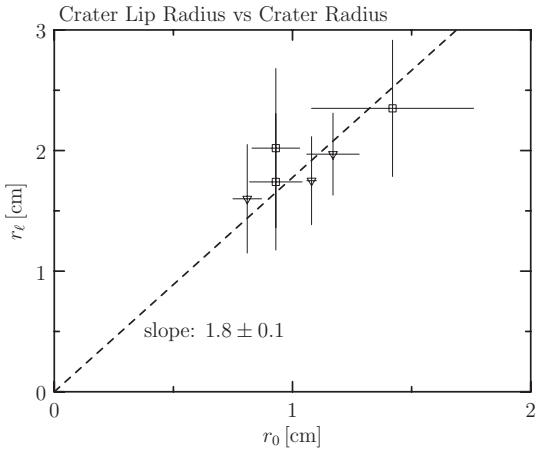

FIG. 10. Radius of the crater lip, r_ℓ, versus the crater radius, r_0, measured for 0.009 cm (downward triangles), and 0.025 cm (squares) ballotini. The best-fit line passing through the origin is indicated by the dashed line. The horizontal error bars represent the error in the measurement of the crater radius; the vertical error bars represent the measured half-width, $\overline{\delta_\ell}$, of the crater lip.

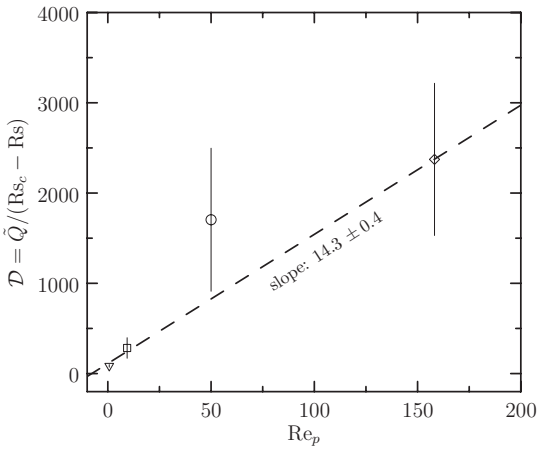

FIG. 11. Change of the nondimensional sediment volume flux with $\mathrm{Rs}_c - \mathrm{Rs}$ plotted versus the particle Reynolds number. Symbols are the same as those shown in Figure 7(a).

Because w_c is approximately constant, the volume flux is constant. It remains to determine how Q depends upon the properties of the particles and the impinging jet.

By analogy with analyses of uniform, statistically steady turbulent flow, we nondimensionalize Q by the particle flux per area density of particles, ${d_p}^2 w_p/(d_p/r_0)^2$. In this definition, we use the measured settling speed, w_p, rather than the inertial settling speed, W_i. Thus the non-dimensional volume flux is defined to be

$$\tilde{Q} \equiv \frac{w_c}{w_p}, \tag{27}$$

which is just the relative crater descent speed, as plotted in Figures 7(a) and 8(a).

If the crater descent rate is relatively slow ($w_c/w_p < 0.002$), the speed of descent, and hence $\tilde{Q}$, increases with $\mathrm{Sh} - \mathrm{Sh}_c$. This is evident by the positively sloped dashed lines in Figure 7(a). The spread in data is insufficient to determine a power law of the form (25). Instead, as a starting point, we suppose w_c/w_p varies linearly with $\mathrm{Sh} - \mathrm{Sh}_c$. From the slopes of the best-fit lines in Figure 7(a), we derive a relationship for relative volume flux upon relative stress of the form (25) with $p = 1$. However, we find that the coefficient varies significantly from values determined for ballotini (ranging from $\mathcal{C}_s = 0.0014$ to 0.0021 from smallest to largest) and for white poppy seeds (with $\mathcal{C}_s \simeq 0.014$). The poorness of the fit is attributed to the scatter of data in Figure 7(a).

Because the definition of Rs explicitly involves the measured settling velocity, we found better collapse of crater-descent data when plotted against Rs than when plotted against Sh. Consequently, we explore whether it is better to express $\tilde{Q}$ in terms of Rs. Explicitly, from the slope of the best-fit lines in Figure 8(a), we determine the deepening speed of the crater relative to w_p as a linear function of $\mathrm{Rs}_c - \mathrm{Rs}$,

$$\tilde{Q} = \mathcal{C}_r(\mathrm{Rs_c} - \mathrm{Rs}). \tag{28}$$

Again we find a large variation of the coefficient $\mathcal{C}_r$ with the different ballotini and poppy seeds. However, unlike the comparison with Shields parameter, here we find that, within errors, $\mathcal{C}_r$ increases approximately linearly with particle Reynolds number for all particle types, as shown in Figure 11.

From the slope of the best-fit line through the data, we propose an empirical relation for the sediment volume flux for low crater deepening rates ($w_c/w_p \lesssim 0.002$) as a function of the Rouse number,

$$\tilde{Q} \simeq (14.3 \pm 0.4)\,\mathrm{Re_p}\,(\mathrm{Rs_c} - \mathrm{Rs}). \tag{29}$$

Together with the definitions (18) and (27), and the formula for the critical Rouse number (22), (29) implicitly relates the crater deepening speed at its center to the centerline speed of the impinging jet

at the particle bed w_j. Explicitly, the deepening speed is

$$w_c \simeq 8.3\, w_p\, \mathrm{Re_p^{3/2}} \left(1 - 4.2 \frac{\mathrm{w_p/w_j}}{\mathrm{Re_p}}\right). \tag{30}$$

Unphysically, this predicts that w_c should reach a finite maximum as $w_j \to \infty$. It is a reminder that the empirical formulas (29) and (30) are only valid for $w_c < 0.002 w_p$ and so for Rs moderately less than Rs_c.

V. DISCUSSION AND CONCLUSIONS

Using light attenuation and depositometer measurements, we have determined the deepening and spread of a crater in a particle bed resulting from an impinging vertical turbulent jet. The initiation of crater formation was determined in terms of a critical Shields parameter, Sh_c, as well as a critical Rouse number, Rs_c. For ballotini, the former decreased with particle Reynolds number, Re_p, as $\mathrm{Sh_c} \propto \mathrm{Re_p^{-0.23}}$. The exponent was smaller than the value -0.5 found for the initiation of particle transport by coherent structures in a vortex ring where the power law behaviour extends beyond $\mathrm{Re}_p \sim 10^2$. The value of Sh_c for the poppy seeds was found to be an order of magnitude smaller than this power law curve determined for ballotini. Conversely, the critical Rouse number was less ambiguously determined and Rs_c was found to vary with Re_p according to $\mathrm{Rs_c} \simeq 0.6\mathrm{Re_p^{0.45}}$ for all particle types for which $0.68 < \mathrm{Re}_p < 160$.

That the critical Rouse number better represented the onset of crater formation with poppy seeds as well as ballotini indicates the importance of the particle settling velocity in understanding bedload transport in non-uniform turbulent flows. A turbulent eddy is able to transport particles in a sediment bed only if it exerts sufficient stress and for long enough to displace particles laterally before they settle back down into the bed.

If a crater formed, the depth at its center was found to increase linearly in time (at constant speed, w_c), while the radius, r_c, remained approximately constant. Bedload transport was measured in terms of the relative crater deepening speed, $\tilde{Q} \equiv w_c/w_p$. The dependency of $\tilde{Q}$ upon the incident jet parameters was best defined in terms of Rs with $\tilde{Q} \simeq 14\mathrm{Re_p}(\mathrm{Rs_c} - \mathrm{Rs})$. Despite scatter in the data, the radial extent of the crater was found to be consistent with the assumption that it is set by the radius of the jet below which the mean vertical speed was larger than the critical speed $w_{j\star}$, which itself is determined from Rs_c.

Although this study examined particle Reynolds numbers spanning two decades, the scatter in results and the relatively small range of particles used in this study make it difficult to draw broad predictions for the formation of craters in sediment layers from impinging vertical jets. The main contribution of this study is to demonstrate that existing empirical predictions used to characterize sediment transport by uniform turbulent flows and by transient coherent structures do not apply to transport by statistically steady turbulent jets. Transport initiation and evolution is better characterized by the Rouse number and particle Reynolds number.

In future studies, experiments will be designed to examine more energetic turbulent jets impinging vertically and at an angle to the vertical upon sediment beds with more widely varying particle sizes and buoyancies. The continuing challenge will be to construct numerical models that can capture the dynamics observed in experiments.

ACKNOWLEDGMENTS

The authors are grateful for the comments of one of the reviewers, whose comments resulted in a reanalysis of the bedload transport using parameters more directly analogous to those used to examine bedload transport in rivers. This work was supported in part by funding from the Natural Sciences and Engineering Research Council Discovery Grant program. The research was conducted while Sutherland was a Churchill Overseas Visiting Fellow at the University of Cambridge.

APPENDIX: THEORY OF TURBULENT JETS

Here we briefly review the theory of statistically steady turbulent jets following the approach of Morton *et al.*,[35] who more generally examined the dynamics of forced turbulent plumes. The theory does not account for details of turbulence within the jet. Rather it characterizes the time-mean behaviour through the solution of equations for the jet speed $w(r, z)$ and characteristic jet radius $b(z)$, in which we arbitrarily assume the jet flows in the z-direction. From these we define the corresponding volume flux, $Q(z) = 2\pi \int_0^\infty wr\, dr$, and momentum flux, $M(z) = 2\pi \int_0^\infty w^2 r\, dr$. (Note, in this Appendix, Q denotes the volume flux of the jet and should not be confused with the particle flux given by (26).) In particular, if one approximates the velocity by a "top-hat" profile such that $w = \bar{w}(z)$ for $r \le b \equiv \bar{b}$ and zero otherwise, the volume and momentum fluxes are

$$Q = \pi \bar{w}\bar{b}^2 \text{ and } \mathrm{M} = \pi \bar{\mathrm{w}}^2 \bar{\mathrm{b}}^2. \tag{A1}$$

If w is assumed more accurately to be radially Gaussian of the form $w = w_g(z)\exp(-r^2/2{b_g}^2)$, then

$$Q = 2\pi w_g {b_g}^2 \text{ and } \mathrm{M} = \pi \mathrm{w_g}^2 \mathrm{b_g}^2. \tag{A2}$$

We make the entrainment assumption[35] that the radial speed of fluid entering the turbulent flow is proportional to the vertical speed of the flow at the centerline, with proportionality constant α. Thus conservation of mass for an incompressible fluid predicts

$$\frac{dQ}{dz} = 2\alpha\sqrt{\pi M}, \tag{A3}$$

and conservation of momentum for a jet with the same density as the uniform-density ambient predicts

$$\frac{dM}{dz} = 0. \tag{A4}$$

Assuming the jet emanates with volume flux Q_0 from a nozzle of radius b_0, the solution of the equations give $Q = Q_0 + (2\alpha\sqrt{\pi M_0})z$ and $M = M_0$ in which, for a top-hat jet, $M_0 = \pi {w_0}^2 {b_0}^2$ and $w_0 = Q_0/(\pi {b_0}^2)$. This gives the radius and mean speed

$$\bar{b}(z) = 2\alpha Z \text{ and } \bar{\mathrm{w}}(\mathrm{z}) = \mathrm{w_0}\frac{\mathrm{b_0}}{2\alpha}\mathrm{Z}^{-1}, \tag{A5}$$

in which $Z = z + z_v$ is the distance from the virtual origin at $z = -z_v \equiv -b_0/(2\alpha)$.

For a Gaussian jet, we find

$$b_g(z) = \alpha Z \text{ and } \mathrm{w_g(z)} = \mathrm{w_0}\frac{\mathrm{b_0}}{\alpha}\mathrm{Z}^{-1}, \tag{A6}$$

in which Z is the distance from the virtual origin now at $z = -z_v \equiv -b_0/\alpha$.

From these results it is clear that one can work with the conceptually easier top-hat relations and then infer the corresponding Gaussian jet properties by setting $b_g = \bar{b}/2$ and $w_g = 2\bar{w}$.

In application of these formulas, we take the entrainment constant for a jet[32,33] to be $\alpha = 0.08$.

[1] H. Masuda, K. Gotoh, H. Fukada, and Y. Banba, "The removal of particles from flat surfaces using a high-speed air jet," Adv. Powder Technol. **5**, 205–217 (1994).
[2] G. T. Smedley, D. J. Phares, and R. C. Flagan, "Entrainment of fine particles from surfaces by gas jets impinging at normal incidence," Exp. Fluids **26**, 324–334 (1999).
[3] G. Ziskind, M. Fichman, and C. Gutfinger, "Particle behavior on surfaces subjected to external excitations," J. Aerosol Sci. **31**, 703–719 (2000).
[4] M. W. Reeks and D. Hall, "Kinetic models for particle resuspension in turbulent flows: Theory and measurement," J. Aerosol Sci. **32**, 1–31 (2001).
[5] R. Fletcher, N. Briggs, E. Ferguson, and G. Gillen, "Measurements of air jet removal efficiencies of spherical particles from cloth and planar surfaces," Aerosol Sci. Technol. **42**, 1052–1061 (2008).
[6] Y.-H. Liu, D. Hirama, and S. Matsusaka, "Particle removal process during application of impinging dry ice jet," Powder Technol. **217**, 607–613 (2012).
[7] F. Zhang, M. Reeks, and M. Kissane, "Particle resuspension in turbulent boundary layers and the influence of non-Gaussian removal forces," J. Aerosol Sci. **58**, 103–128 (2013).
[8] L. Biasi, A. de los Reyes, M. W. Reeks, and G. F. de Santi, "Use of a simple model for the interpretation of experimental data on particle resuspension in turbulent flows," Aerosol Sci. **32**, 1175–1200 (2001).

[9] K. W. Nicholson, "A review of particle resuspension," Atmos. Env. **22**, 2639–2651 (1988).
[10] D. E. Drake and D. A. Cacchione, "Field observations of bed shear stress and sediment resuspension on continental shelves, Alaska and California," Cont. Shelf Res. **6**, 415–429 (1986).
[11] B. Gomez, "Bedload transport," Earth-Sci. Rev. **31**, 89–132 (1991).
[12] B. M. Sumer, L. H. C. Chua, N.-S. Cheng, and J. Fredsøe, "Influence of turbulence on bed load sediment transport," J. Hydraul. Eng. **129**, 585–596 (2003).
[13] E. Y. Spahn, A. R. Horner-Devine, J. D. Nash, and D. A. Jay, "Particle resuspension in the Columbia River plume near field," J. Geophys. Res. **114**, C00B14, doi:10.1029/2008JC004986 (2009).
[14] S. A. Miedema, "Constructing the Shields curve. Part A: Fundamentals of the sliding, rolling and lifting mechanisms for the entrainment of particles," J. Dredging Eng. **12**, 1–49 (2012).
[15] S. A. Miedema, "Constructing the Shields curve. Part B: Sensitivity analysis, exposure and protrusion levels settling velocity, shear stress and friction velocity, erosion flux and laminar main flow," J. Dredging Eng. **12**, 50–92 (2012).
[16] L. Boegman and G. N. Ivey, "Flow separation and resuspension beneath shoaling nonlinear internal waves," J. Geophys. Res. **114**, C02018, doi:10.1029/2007JC004411 (2009).
[17] D. B. Reeder, B. B. Ma, and Y. J. Yang, "Very large subaqueous sand dunes on the upper continental slope in the South China Sea generated by episodic, shoaling deep-water internal solitary waves," Marine Geol. **279**, 12–18 (2011).
[18] B. R. Sutherland, K. J. Barrett, and G. N. Ivey, "Shoaling internal solitary waves," J. Geophys. Res. **118**, 1–14, doi:10.1002/jgrc.20291 (2013).
[19] G. Ziskind, M. Fichman, and C. Gutfinger, "Resuspension of particulates from surfaces to turbulent flows – Review and analysis," J. Aerosol Sci. **26**, 613–644 (1995).
[20] J. M. Redondo, X. D. de Madron, P. Medina, M. A. Sanchez, and E. Schaaff, "Comparison of sediment resuspension measurements in sheared and zero-mean turbulent flows," Cont. Shelf Res. **21**, 2095–2103 (2001).
[21] Y. Niño, F. Lopez, and M. Garcia, "Threshold for particle entrainment into suspension," Sedimentology **50**, 247–263 (2003).
[22] A. N. Papanicolaou, M. Elhakeem, G. Krallis, S. Prakash, and J. Edinger, "Sediment transport modeling review – Current and future developments," J. Hydraul. Eng. **134**, 1–14 (2008).
[23] M. M. Stempniewicz, E. M. J. Komen, and A. de With, "Model of particle resuspension in turbulent flows," Nuclear Eng. Design **238**, 2943–2959 (2008).
[24] A. Shields, "Anwendung der Aehnlichkeitsmechanick und der Turbulenzforschung auf die Geschiebebewegung," Mitt. Preuss. Vers. Wasser. Schiff. (1936).
[25] A. J. Sutherland, "Proposed mechanism for sediment entrainment by turbulent flows," J. Geophys. Res. **72**, 6183–6194, doi:10.1029/JZ072i024p06183 (1967).
[26] I. Eames and S. B. Dalziel, "Dust resuspension by the flow around an impacting sphere," J. Fluid Mech. **403**, 305–328 (2000).
[27] R. J. Munro, N. Bethke, and S. B. Dalziel, "Sediment resuspension and erosion by vortex rings," Phys. Fluids **21**, 046601 (2009).
[28] N. Bethke and S. B. Dalziel, "Resuspension onset and crater erosion by a vortex ring interacting with a particle layer," Phys. Fluids **24**, 063301 (2012).
[29] R. J. Munro and S. B. Dalziel, "Attenuation technique for measuring sediment displacement levels," Exp. Fluids **39**, 600–611 (2005).
[30] F. de Rooij, S. B. Dalziel, and P. F. Linden, "Electrical measurement of sediment layer thickness under suspension flows," Exp. Fluids **26**, 470–474 (1999).
[31] M. Konz, P. Ackerer, P. Huggenberger, and C. Veit, "Comparison of light transmission and reflection techniques to determine concentrations in flow tank experiments," Exp. Fluids **47**, 85–93 (2009).
[32] B. R. Morton, "Forced plumes," J. Fluid Mech. **5**, 151–163 (1959).
[33] N. B. Kaye, "Turbulent plumes in stratified environments: A review of recent work," Atmos.-Oceans **46**, 433–441 (2008).
[34] C. M. Choux and T. H. Druitt, "Analogue study of particle segregation in pyroclastic density currents, with implications for the emplacement mechanisms of large ignimbrites," Sedimentology **49**, 907–928 (2002).
[35] B. R. Morton, G. I. Taylor, and J. S. Turner, "Turbulent gravitational convection from maintained and instantaneous sources," Proc. R. Soc. London, Ser. A **234**, 1–23 (1956).
[36] L. van Rijn, "Sediment transport. Part I: Bed load transport," J. Hydraul. Eng. **110**, 1431–1456 (1984).
[37] R. J. Munro and S. Dalziel, personal communication (2013).